# Turbulent Drag Reduction at High Reynolds Number

I. Marusic[1], D. Chandran[1], A. Rouhi[2], M. K. Fu[3], A. Zampiron[4],
D. Wine[5], B. Holloway[5], and A. J. Smits[6]
([1]University of Melbourne, AU, [2]Nottingham Trent University, UK,
[3]Caltech, USA, [4]University of Aberdeen, UK,
[5]Intellectual Ventures, USA, [6]Princeton University, USA)

## ABSTRACT

We present direct measurements of substantial drag reduction at friction Reynolds numbers ($\mathrm{Re}_\tau$) up to 12,800 using spanwise surface oscillations. These measurements were achieved in the high Reynolds number turbulent boundary layer wind tunnel at the University of Melbourne using a custom actuation system that generated an upstream traveling wave of spanwise wall-oscillations via moving slats. The drag reduction was measured via a combination of drag balance and hot-wire anemometry, and was paired with matched large-eddy simulations to identify the Reynolds number trends for fixed sets of actuation parameters. The drag reduction was found to occur via two distinct physical pathways. The first pathway, recognised by previous studies, involved actuating the surface at high frequencies, comparable to those of the small-scale eddies that dominate turbulence near the surface. This approach generated drag reduction levels up to 25% at $\mathrm{Re}_\tau$ = 6,000, consistent with previous predictions based on much lower Reynolds numbers, albeit with an estimated net power cost of 20-25%. The second pathway, however, was new and leveraged actuation at low frequencies comparable to those of the large-scale eddies farther from the surface. The measured drag reduction greatly exceeded all prior predictions for these parameters, producing drag reduction of 13% at $\mathrm{Re}_\tau$ = 12,800 with an estimated net power savings of up to 8%. Drag reduction obtained through this pathway, importantly, increased with Reynolds number, thereby opening up an unexpected, new avenue for reducing fuel consumption by transport vehicles.

## INTRODUCTION

Turbulent skin-friction drag limits the speed and efficiency of many critical transportation and energy systems, including airplanes, ships, and wind turbines. For example, about $50\%$ of the fuel on a typical commercial airplane flight is spent overcoming skin friction drag. An economic analysis by Schultz et al. (2011) estimates that the cost associated with hull fouling for the Navy's current hull husbandry practices totals \$56M per year or \$1.0B over 15 years for the entire DDG-51 class. Even a modest drag reduction under conditions relevant to real-world applications would therefore be environmentally and economically significant. However, our ability to identify and model efficient strategies for reducing skin-friction drag has been limited by the wide range of turbulent flow scales inherent to these systems and their nonlinear interactions.

One of the most promising actuation methods for significantly reducing drag has been spanwise oscillation of surface elements synchronized to produce a traveling wave in the direction opposing the fluid stream, such as that illustrated in Figure 1. The sinusoidal oscillation is prescribed by

$$w_s(x,t) = A\sin(\kappa_x x - \omega t), \tag{1}$$

where $w_s$ is the spanwise velocity of the surface, $A$ is the amplitude of the spanwise velocity of each element, $\omega$ is the spanwise frequency, and $\kappa_x = 2\pi/\lambda$ is the wavenumber of the traveling wave. While there are obvious practical obstacles to using oscillating elements on the surface of vehicles to reduce drag, the physical insights that can be revealed through this method warrant closer examination.

For this actuation strategy, the mean wall stress has a functional dependence on the various actuation and flow parameters (shown in Figure 1) as:

$$\frac{\overline{\tau_w}}{\rho} = u_\tau^2 = g_1(U_\infty,\, \delta,\, \nu,\, \kappa_x,\, \omega,\, A) \tag{2}$$

where $U_\infty$ is the freestream velocity, $\delta$ is the boundary

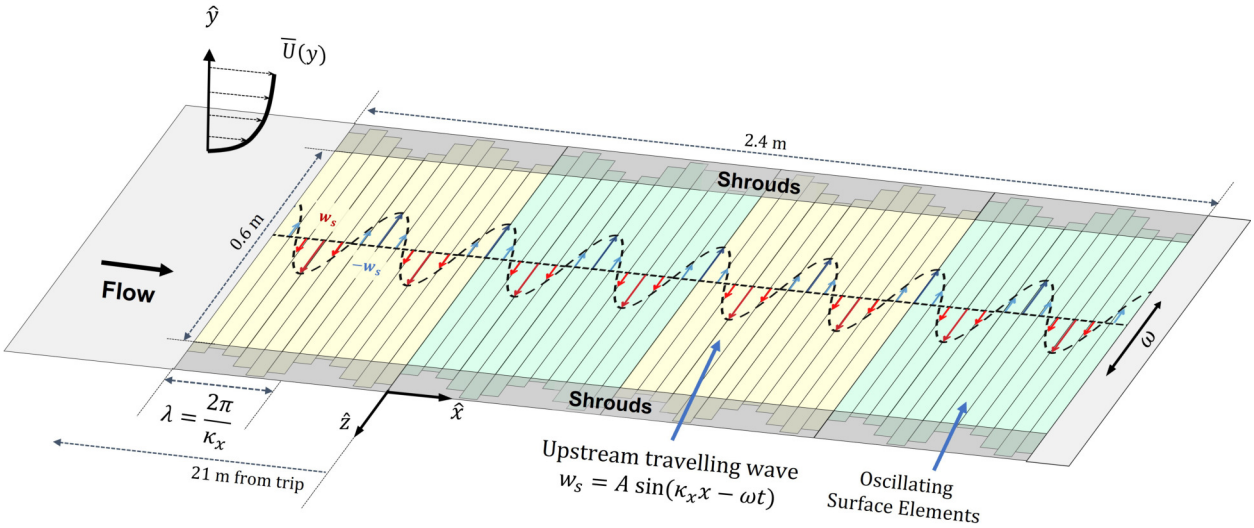


**Figure 1:** Diagram of the actuation scheme. Sliding elements embedded in the surface were oscillated synchronously at a frequency $\omega$ to create an upstream traveling wave of spanwise velocity $w_s$ and wavelength $\lambda$. Here, $x$, $y$ and $z$ denote streamwise, wall-normal and spanwise coordinates, respectively.

layer thickness, $\nu$ is the fluid kinematic viscosity, and the friction velocity $u_\tau \equiv \sqrt{\overline{\tau_w}/\rho}$, $\rho$ being the fluid density. The drag reduction (DR) stemming from active flow control is measured as the fractional decrease in $\overline{\tau_w}$, the time-averaged local drag force per unit area acting on the surface or "wall", as given by

$$\mathrm{DR} = \left(1 - \frac{\overline{\tau_w}}{\overline{\tau_{w0}}}\right). \tag{3}$$

Here, $\overline{\tau_w}$ is often referred to as the mean wall stress. Throughout this report, overbars indicate a long-time average, and $\overline{\tau_{w0}}$ denotes the mean wall stress acting on the non-actuated, i.e., stationary, surface.

Equations 2 and 3 allows us to express DR as a function of three dimensionless actuation parameters and the Reynolds number as :

$$\mathrm{DR} = g_2(\kappa_x^+,\, T_{\mathrm{osc}}^+,\, A^+,\, \mathrm{Re}_\tau) \tag{4}$$

where $\kappa_x^+ = \kappa_x\, \nu / u_{\tau 0}$ (here $u_{\tau 0} \equiv \sqrt{\overline{\tau_{w0}}/\rho}$), $T_{osc}^+ = 2\pi\, u_{\tau 0}^2 / (\omega\nu)$, and $A^+ = A/u_{\tau 0}$ are the dimensionless actuation parameters and $\mathrm{Re}_\tau$ is the friction Reynolds number, $\mathrm{Re}_\tau = \delta u_{\tau 0}/\nu$. In this manuscript, the '+' superscript refers to inner-scaled normalization based on the *non-actuated* flow using the viscous length scale $\eta_v \equiv \nu/u_{\tau 0}$ and friction velocity $u_{\tau 0}$.

To date, nearly all previous investigations of this active flow control method have focused on parameterizing how the drag reduction depends on the three dimensionless actuation parameters $\kappa_x^+$, $T_{osc}^+$, and $A^+$ (see, for example, Ricco et al. (2021)) in low-speed and viscous-flow applications that are feasible within lab experiments and numerical simulations, i.e., $\mathrm{Re}_\tau \leq 1{,}000$ (Jung et al., 1992; Choi and Graham, 1998; Schoppa and Hussain, 1998; Iwamoto et al., 2005; Quadrio et al., 2009; Viotti et al., 2009; Auteri et al., 2010; Nakanishi et al., 2012; Tomiyama and Fukagata, 2013; Yakeno et al., 2014; Gatti and Quadrio, 2016; Meysonnat et al., 2016; Bird et al., 2018a,b; Yao et al., 2019; Skote et al., 2019). In this regime, the most effective drag reduction pathways were found to be those that target and control the near-surface, small-scale eddies that dominate the surface stresses (Ricco et al., 2021).

The physics behind this strategy of targeting the small-scale eddies can be understood by examining Figure 2, which shows the power spectral density of wall shear stress ($\phi_{\tau\tau}^+$) as a function of $T^+ = 1/f^+ = u_{\tau 0}^2/(f\nu)$, where $f$ is frequency. In this case, the power spectral density is shown in its pre-multiplied form, $f^+\phi_{\tau\tau}^+$, for a stationary wall condition at $\mathrm{Re}_\tau = 10^3$, $10^4$, and $10^5$ to illustrate the contribution of turbulent structures with different time scales ($T^+$) to the wall shear stress. The spectra at $\mathrm{Re}_\tau = 10^3$ and $\mathrm{Re}_\tau = 10^4$ were computed from direct numerical simulation (DNS) of a channel flow (Del Álamo et al., 2004) and our hot-wire data, respectively, while the spectra at $\mathrm{Re}_\tau = 10^5$ is a prediction based on the models of Marusic et al. (2010), Mathis et al. (2013), and Chandran et al. (2020), and is included to indicate the expected trend with increasing Reynolds number.

We see that each spectrum in Figure 2 (given by a solid black or gray line) features a strong peak at $T^+ = 80 - 100$, reflecting the intense high-frequency turbulence generated by the near-wall streaks. Furthermore, as reported by Mathis et al. (2013) and Marusic et al. (2010), the contributions from turbulent small-scales $T^+ \lesssim 350$ are universal and do not change with Reynolds number. Consequently, drag reduction approaches at low Reynolds numbers need to target the small eddies near the surface

because these eddies contribute most of the drag. When this type of actuation is employed it is often seen to modify the mean velocity profile through a Reynolds number-invariant additive constant, $\Delta B^+$, implying that the actuation is primarily acting on turbulent structures in the near wall region and that the outer flow effectively perceives the modified inner layer as a lower stress. Gatti and Quadrio (2016) used this assumption to propose the modified friction law:

$$\Delta B^+ = \sqrt{\frac{2}{C_{f,0}}}\left[\frac{1}{\sqrt{(1-\mathrm{DR})}} - 1\right] - \frac{1}{2\kappa}\ln\left(1-\mathrm{DR}\right) \tag{5}$$

where $C_{f,0} \equiv \overline{\tau_{w0}}\left(\frac{1}{2}\rho U_\infty^2\right)^{-1}$ is the friction factor of the non-actuated surface, and $\kappa$ is the von Kármán constant. In this framework, all of the Reynolds number dependence of the flow is captured by $C_{f,0}$, provided that there is a well-defined logarithmic layer in the mean velocity profile. The behavior of the log-layer is modified by the actuation solely through the offset parameter, $\Delta B^+$, that can parameterized by the dimensionless actuation parameters.

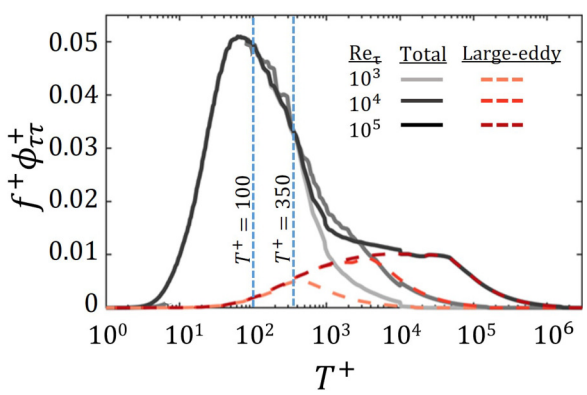


**Figure 2:** Pre-multiplied spectra ($f^+\phi^+_{\tau\tau}$) of the wall stress ($\tau_w$) with inner-scaling is shown as a function of time scale, $T^+$, for a stationary wall at $\mathrm{Re}_\tau = 10^3$, $10^4$, and $10^5$. The spectra were composed using the predictive models of Marusic et al. (2010), Mathis et al. (2013), and Chandran et al. (2020). The solid black lines indicate the total spectrum and the dashed red lines indicate the contribution to the total from outer-region large-scale structures, which is Reynolds number dependent. Vertical blue lines are included to indicate the locations of $T^+ = 100$ and $T^+ = 350$. See Marusic et al. (2021) for more details.

Unfortunately, targeting these small-eddies, especially at higher Reynolds numbers, can be challenging, requiring very high actuation frequencies and wavenumbers (Quadrio et al., 2009; Smits et al., 2011; Jiménez, 2018). Many practical constraints limit the applicability of this approach, including insufficient actuation (Cattafesta and Sheplak, 2011), engineering complexity, and capital costs (Leschziner et al., 2011), and can prevent experimental validation of otherwise theoretically promising drag reduction strategies. Only a handful of experiments (e.g., Auteri et al., 2010; Bird et al., 2018b), all at $\mathrm{Re}_\tau < 1000$, have been performed for wall oscillations with streamwise modulation and exist as a testament to the formidable experimental challenges. Even in these cases, the empirical results have limited agreement with the numerical models, and various geometry and impedance issues have been proffered to explain the discrepancies. Successfully extending these strategies and models (e.g., equation 5) to application-relevant conditions (i.e., high Reynolds numbers) has never been achieved.

We propose an alternative actuation scheme for high Reynolds numbers that couples to large-scale eddies and still achieves substantial drag reduction while also requiring much lower actuation frequencies. At higher Reynolds numbers, the physics of drag generation evolves as the larger, outer-layer motions make an increasingly significant contribution to turbulent transport and skin-friction (Fukagata et al., 2006). This shift manifests itself as the $\mathrm{Re}_\tau$ trend at large-scales ($T^+ > 350$) shown in Figure 2 using red-dashed lines according to the decomposition of Mathis et al. (2013), Chandran et al. (2020), and Marusic et al. (2010). Unlike the small-eddy component, these "large-eddy" contributions increase with Reynolds number, i.e., the ratio of area under red-dashed curve to the area under the solid black curve in Figure 2, from about $8\%$ of the total variance at $\mathrm{Re}_\tau = 10^3$ to about $30\%$ at $\mathrm{Re}_\tau = 10^5$. This trend indicates the increased superimposition and modulation of the energetic large-scale motions that occur in the outer region of the boundary layer on the small-scale motions that occur in the near-wall region (Hutchins and Marusic, 2007; Mathis et al., 2009; Marusic et al., 2010; Agostini and Leschziner, 2018, 2019). Towards this end, we will adopt the demarcation threshold of $T^+ = 350$ following Mathis et al. (2013) and refer to turbulent scales and actuation periods associated with $T^+ < 350$ as "small-eddy" and $T^+ > 350$ as "large-eddy."

In this study, we conducted direct measurements of drag reduction using spanwise surface oscillations up to $\mathrm{Re}_\tau = 12,800$. To the best of our knowledge, all previous numerical and experimental studies in this space were limited to Reynolds numbers $\mathrm{Re}_\tau < 1000$, at least an order of magnitude lower than our current capability. The drag reduction obtained in this study was found to occur via two distinct physical pathways. The first pathway was the "small-eddy" actuation strategy noted in previous studies, where the surface was actuated at frequencies comparable to those of the small-scale eddies that dominate turbulence near the surface. Consistent with previous studies (Gatti and Quadrio, 2016), the drag reduction was substantial but found to diminish with

$\mathrm{Re}_\tau$ with an inherent power cost that exceeded any drag reduction savings. The second pathway was new (see Marusic et al., 2021) and involved actuating at frequencies comparable to those of the large-scale eddies farther from the surface. This "large-eddy" manipulation pathway was not only estimated to require significantly less power but the drag reduction was shown to increase with Reynolds number.

These measurements were achieved through the wide-ranging capabilities of the University of Melbourne's large-scale turbulent boundary layer facility combined with a unique surface actuation test-bed (SATB) capable of actuating a large portion of the tunnel boundary layer with spanwise wall oscillations. Because the actuator was designed and manufactured to a high degree of precision, the machine surface was able to execute significant spanwise motions while effectively being an otherwise smooth surface, with minimal out-of-plane motion and negligible gaps and steps between slats.

The friction drag on the actuated surface was measured via two independent experimental techniques: 1) directly with a large-scale drag balance and 2) indirectly with a single-wire hot-wire anemometer. For the drag balance measurements, the SATB was mounted flush to the tunnel wall on a large floating element that was effectively frictionless for streamwise displacements. The integrated, streamwise drag force acting on the entire exposed floating element surface, nearly half of which was actuated, was measured directly by a load cell (Baars et al., 2016), while hot-wire anemometry was employed to determine the local skin friction over the actuator surface. The combined capabilities allowed us to actuate the turbulent structures over a wide range of spatio-temporal scales and Reynolds numbers, and quantify their effects with a high degree of precision and certainty.

To determine how DR varies with $\mathrm{Re}_\tau$, we need to operate with fixed values of the dimensionless actuation parameters $\kappa_x^+$, $T_{\mathrm{osc}}^+$ and $A^+$, as shown in Equation 4. However, due to the limits on operational envelope of the SATB and wind tunnel, it is not possible to match the dimensionless actuation parameters over the entire Reynolds number range. To alleviate these constraints, we paired our experimental results with a series of complementary large-eddy simulations (LES) at $\mathrm{Re}_\tau \leq$ 2,000. These numerical tools also helped to provide key insights into the drag reduction mechanisms associated with small- and large-eddy actuation.

## METHODOLOGY

### High Reynolds Number Boundary Layer Wind Tunnel

Experiments were performed in the high Reynolds number boundary layer wind tunnel facility (HRNBLWT) at the University of Melbourne. The tunnel test section is over 27 m long and features a 2 m $\times$ 1 m cross-section. A canonical turbulent boundary layer was produced by tripping the flow at the entrance to the test section with a 35 mm wide stripe of P40 grit sandpaper (425–500 µm grit size). A zero-pressure gradient condition was maintained by bleeding off the top wall boundary layer. The mean freestream velocity throughout the entire working section was constant to within $\pm 0.5\%$ for all locations and test conditions evaluated here, with free-stream turbulence intensities $(u_{rms}/U_\infty) < 0.2\%$. All experiments in this study were performed at a streamwise location of $x \approx$ 21 m, where the turbulent boundary layer thickness was $\delta \approx 390$ mm. The friction Reynolds numbers were varied over the range 6,000 to 12,800 by varying the freestream velocity from 7 to 15 m/s. The experimental conditions are summarized in Table 1. More details on the facility are given by Baars et al. (2016).

### Surface actuation test bed (SATB)

The surface actuation test bed (SATB) was custom designed and built to actuate the high-Reynolds number boundary layer with spanwise wall oscillation frequencies up to $f = \omega/(2\pi) = 25$ Hz. The SATB, diagrammed in Figure 1, actuated the overlying flow with a series of forty-eight, 50 mm-wide slats that oscillated sinusoidally in time in the spanwise direction with a fixed half-stroke length, $d = 18$ mm, and a maximum spanwise velocity $A = \omega d$, so that the spanwise velocity and oscillation frequency are inherently coupled. The slat oscillation was driven by four independently controlled machines placed end-to-end along the length of the drag balance floating element.

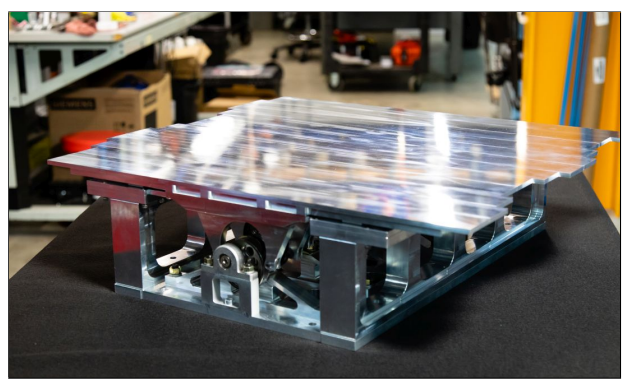

**Figure 3:** Photograph of one of the four surface-actuation test bed (SATB) machines looking down the streamwise direction. The $2\lambda$ of streamwise traveling wave generated by this machine can be seen in the slat displacement at the edge of the machine.

Each machine (see Figure 3) had 12 slats whose phase was controlled by a central camshaft. The sinusoidal traveling wave was discretized with six slats constituting a fixed streamwise wavelength $\lambda = 2\pi/\kappa_x =$ 0.3 m (Auteri et al., 2010). The four machines were

**Table 1** Details of the flow conditions and chosen actuation parameters for the experiments and LES. The experimental methods include hot-wire (HW) and drag balance (DB). The symbols in the table correspond to Figures 4 and 7. Each set of actuation parameters is dubbed either small-eddy, intermediate, or large-eddy based on whether $T^+_{\rm osc} < 350$, $T^+_{\rm osc} \approx 350$, or $T^+_{\rm osc} > 350$, respectively.

| Name | Actuation | | | Experiment | | | | | | LES | |
|---|---|---|---|---|---|---|---|---|---|---|---|
| | $T^+_{osc}$ | $A^+$ | $\kappa^+_x$ | Method | Sym. | $\mathrm{Re}_\tau$ | $U_\infty$(m/s) | $f$(Hz) | $A$(m/s) | Sym. | $\mathrm{Re}_\tau$ |
| Small-eddy | 140 | 12 | 0.0014 | HW, DB | ●, ▲ | 6000 | 7 | 25 | 2.83 | □ | 951, 2003 |
| Intermediate | 348 | 4.9 | 0.0014 | HW | ● | 6000 | 7 | 10 | 1.13 | □ | 951, 2003 |
| | 362 | 7.8 | 0.0008 | HW, DB | ●, ▲ | 9700 | 11 | 25 | 2.83 | □ | 951, 2003 |
| Large-eddy | 604 | 4.6 | 0.0008 | HW, DB | ●, ▲ | 9700 | 11 | 15 | 1.7 | □ | 951, 2003 |
| | 653 | 5.7 | 0.0006 | DB | ▲ | 12800 | 15 | 25 | 2.83 | | |
| | 1100 | 3.5 | 0.0006 | DB | ▲ | 12800 | 15 | 15 | 1.7 | □ | 951, 2003 |

driven by servomotors that were phase synchronized to ensure a continuous $8\lambda$ long upstream traveling wave of spanwise velocity. For all experiments presented here, the streamwise traveling wave was driven in the upstream direction to avoid any phase locking between the near-wall structures and actuation, which can lead to drag increase, and increase the effective actuation frequency experienced by the turbulent structures as they convect downstream (see Quadrio et al., 2009).

The chamber below the floating element was pressurized to match the static pressure of the tunnel working section. This pressurization eliminated any flow leakage through the $\mathcal{O}(100$ µm$)$ gaps between the slats. The flatness and vertical displacement of the slats were measured using a laser displacement sensor (Keyence LK-031, $\pm 1$ µm accuracy, 30 µm beam diameter). The maximum step height between slats in the stationary configuration and the peak-to-peak vertical displacement of individual slats during oscillations were both typically $\mathcal{O}(10$ µm$)$ for most slats and $\mathcal{O}(100$ µm$)$ in the worst case. These vertical displacements are associated with the disparities and motions of individual slats rather than the specific operating frequency of the machine. Importantly, the flow measurements obtained over the stationary SATB were found to agree well with the smooth wall measurements previously obtained in the facility.

### Hot-wire anemometry

For a given location on the wall, the instantaneous, streamwise wall shear stress on the surface, $\tau_w$, is given by

$$\frac{\tau_w}{\rho} = \nu \frac{\partial U(y)}{\partial y}\bigg|_{y=0}. \tag{6}$$

For a turbulent wall-bounded flow, the velocity gradient at the surface can be approximated to within a few percent error (Hutchins and Choi, 2002) by measuring the streamwise velocity in close proximity to the wall so that

$$\frac{\tau_w}{\rho} = \nu \frac{U(y)}{y} + \mathcal{O}(y) \ : \ y^+ \leq 10. \tag{7}$$

In our experiment, $\tau_w$ was therefore found by measuring the velocity using a hot wire placed at $y^+ \approx 5$ ($y = 370$ µm and 200 µm for the $\mathrm{Re}_\tau = 6{,}000$ and 9,700 cases, respectively). The results were consistent with additional measurements at other wall-normal locations for $y^+ \leq 10$.

The hot-wire sensors were fabricated from Wollaston wires that were soldered to Dantec boundary-layer type miniature prongs. The wires were etched to reveal a 0.5 mm long, 2.5 µm diameter platinum sensing element. The probes were operated with an in-house Melbourne University Constant Temperature Anemometer (MUCTA) circuit at an overheat ratio of 1.8. The resulting frequency response was 20 kHz based on the -3 dB cut-off as verified using a square-wave test. The signals were sampled at 40 kHz ($f^+ = f\,\nu\,u_\tau^{-2} = 11.5$) and 50 kHz ($f^+ = 5.5$), respectively at $\mathrm{Re}_\tau \approx$ 6,000 and 9,700, and low-pass filtered using an 8-pole Butterworth filter (Frequency Devices, Inc. model 9002) with the roll-off set at half the sampling frequency to avoid aliasing. The signals were sampled for $t = 60 - 90$ seconds at each location such that the non-dimensional boundary layer turnover times ($tU_\infty/\delta$) associated with the largest structures in the flow were 1,100 to 2,500. This period of operation ensured sufficiently converged statistics while still preserving the service life of the SATB. The probe response was calibrated in the tunnel freestream at 15 different velocities and fit with a third-order polynomial. The hot-wire probe was positioned in close proximity to the wall using a stepper motor-driven vertical traverse equipped with a linear optical

encoder (RENISHAW RGH24-type, $\pm 0.5$ μm accuracy). The absolute displacement of the probe measurement was validated using a depth measuring displacement microscope (Titan Tool Supply, $\pm 1$ μm accuracy). Further details of how the drag reduction was computed from the hot-wire anemometry can be found in Marusic et al. (2021).

### Drag balance

In addition to acquiring the local wall stress using hot-wire anemometry, the area-averaged drag force was obtained by mounting the entire actuation system on a large floating element drag balance. The exposed surface of the floating element measured 3 m $\times$ 1 m. A series of air bearings were used to restrict spanwise motion of the element while allowing for nearly frictionless movement in the streamwise direction. Streamwise displacement of the floating element was constrained by a 6 N load cell ($0.06\%$ accuracy full scale). The SATB was flush mounted in a 2.7 m $\times$ 0.7 m cutout in the surface, so that it occupied about $48\%$ of the entire floating element surface, with an additional $8\%$ of floating element surface located immediately downstream of the actuator where latent drag reduction effects could have been present. Further details on the construction, calibration, and validation of the floating element system can be found in Baars et al. (2016).

### Computational method

Wall-resolved, large-eddy simulation (LES) of channel flow was employed with matched dimensionless actuation parameters to the experiments at friction Reynolds numbers $\mathrm{Re}_\tau = 951$ and 2003. The dynamic Smagorinsky model (Germano et al., 1991; Lilly, 1992) was used as the subgrid-scale model and was validated at lower Reynolds numbers against the direct numerical simulation (DNS) of Gatti and Quadrio (2016) where data was available. The solver was a fourth-order accurate finite-difference code (Chung et al., 2014, 2015) on a periodic open channel domain with the size $(L_x,\, L_y,\, L_z) \simeq (6h, h, 3h)$. The wall-normal flow scales were resolved down to the viscous sublayer at the bottom wall (no wall modeling) with a streamwise and spanwise grid spacing, $[\Delta_x^+, \Delta_z^+]$, of $[62, 31]$ and $[30, 15]$ for the small-eddy actuation and the large-eddy actuation cases, respectively. For each set of $[A^+, T_{osc}^+, \kappa_x^+]$, grid convergence tests were conducted until the change in the percent drag reduction $\mathrm{DR}_\tau$ was less than $2\%$. Further details of the grid are given in Table 2.

**Table 2** Domain and resolution parameters for the large-eddy simulations (LES).

| $\mathrm{Re}_\tau$ | Actuation | $[\Delta_x^+,\, \Delta_z^+]$ | $N_x \times N_y \times N_z$ |
|---|---|---|---|
| 951 | Small-eddy | [62, 31] | $144 \times 48 \times 96$ |
| 951 | Intermediate | [30, 15] | $264 \times 96 \times 192$ |
| 951 | Large-eddy | [30, 15] | $280 \times 96 \times 192$ |
| 2003 | Small-eddy | [62, 31] | $224 \times 96 \times 192$ |
| 2003 | Intermediate | [30, 15] | $470 \times 200 \times 400$ |
| 2003 | Large-eddy | [30, 15] | $590 \times 200 \times 400$ |

## RESULTS

The drag reduction results, as reported initially in Marusic et al. (2021), are shown in Figure 4. They are parsed into three actuation categories: small-eddy, intermediate, and large-eddy shown in Figure 4(a)-(c), respectively. Following the decomposition proposed by Mathis et al. (2013) and Marusic et al. (2021), small-eddy and large-eddy actuation refer to actuation occurring on time scales comparable to the smaller, near-wall motions ($T_{\mathrm{osc}}^+ \approx 100$) and the larger, outer-region motions ($T_{\mathrm{osc}}^+ > 350$), respectively. The intermediate category was actuation where the oscillation period was comparable to the large-scale cut-off ($T_{\mathrm{osc}}^+ \approx 350$).

### Small-eddy actuation

For the small-eddy actuation, the actuation parameters $[A^+ = 12,\ T_{\mathrm{osc}}^+ = 140$ and $\kappa_x^+ = 0.0014]$ were selected to be nominally optimal for controlling the near-wall motions, based on previous work (Gatti and Quadrio, 2016; Jung et al., 1992). With these actuation parameters we measured $\mathrm{DR}_\tau \approx 25\%$ at a $\mathrm{Re}_\tau =$ 6,000, which represents only a modest decrease from the 30% level found by Gatti and Quadrio (2016) using DNS at $\mathrm{Re}_\tau \approx$ 1,000, and by our LES at $\mathrm{Re}_\tau = 951$. Note that the DR values obtained by hot-wire anemometry and by using the drag balance agreed to within the experimental uncertainty. Here, the error bars correspond to a one standard deviation estimated uncertainty range as determined from at least three independent measurements.

This trend of decreasing DR with increasing Reynolds number has been extensively discussed in the literature (see for example the recent review paper by Ricco et al. (2021)) and we see from Figure 4 that it is well captured by the predictive model of Gatti and Quadrio (2016). This model adopts a Reynolds number invariant shift in the inner-scaled mean velocity profile due to the actuation. This approach effectively assumes that DR depends only on the actuation parameters scaled with inner variables based on the local wall stress at a given Reynolds number. Taken together, the results in Figure 4(a) confirm that small-eddy actuation can offer

an effective drag reduction strategy even at high Reynolds numbers. However, this level of drag reduction can come at a substantial cost in power, as will be discussed below.

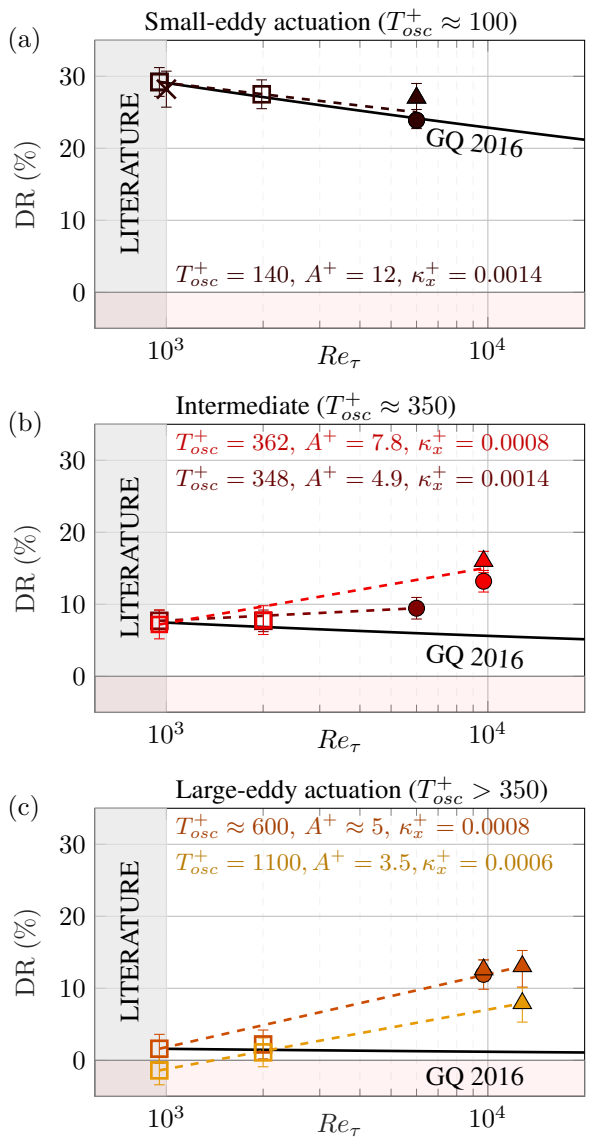


**Figure 4:** DR as a function of $\mathrm{Re}_\tau$ using (a) small-eddy, (b) intermediate, and (c) large-eddy actuation parameters. (□): LES results; (●): hot-wire measurements; (▲): drag balance results; (×): direct-numerical simulation (DNS) result of Gatti and Quadrio (2016); (▬) labeled with "GQ2016": prediction from the model of Gatti and Quadrio (2016) given by equation 5. Error bars indicate one standard deviation estimated uncertainty ranges based on average measurements from independent experiments. Red-shaded area indicates the region of drag increase (DR $< 0$) and the white region, drag reduction (DR $> 0$). Dashed lines (– –) connecting experimental and computational results serve as a visual aid only. Figures are adapted from Marusic et al. (2021).

### Large-eddy actuation

Large-eddy actuation results are shown in Figure 4(c) for two sets of parameters: [$A^+ = 4.6$, $T^+_{\mathrm{osc}} = 604$, $\kappa^+_x = 0.0008$] and [$A^+ = 3.5$, $T^+_{\mathrm{osc}} = 1100$, $\kappa^+_x = 0.0006$]. Although these parameters were constrained by the operational envelope of the SATB and the wind tunnel, they are distinguished by having comparatively large values of $T^+$.

For the first set of actuation parameters Figure 4(c) where $T^+_{\mathrm{osc}} \approx 600$, very little drag reduction is seen at low Reynolds numbers; only DR $= 1.6\%$ at $\mathrm{Re}_\tau = 951$. Under the same operating conditions at $\mathrm{Re}_\tau = 12{,}800$, however, we obtained DR $\approx 13\%$. This value is an order of magnitude higher than that expected on the basis of previous predictions (Gatti and Quadrio, 2016), and, most importantly, for a fixed set of actuation parameters the drag reduction increases with Reynolds number, contrary to such prior predictions. For the second set of actuation parameters in Figure 4(c) where $T^+_{\mathrm{osc}} \approx 1100$, a similar trend is seen. There, the longer period and lower amplitude of oscillation yielded DR $= -1.4\%$ at $\mathrm{Re}_\tau = 951$ (a drag increase), but DR $= 8\%$ at $\mathrm{Re}_\tau = 12{,}800$. We thus conclude that large-eddy actuation can lead to substantial drag reduction and is a promising approach for high Reynolds number applications.

### Intermediate-eddy actuation

For the two intermediate actuation cases where $T^+_{\mathrm{osc}} \approx 350$ (see Figure 4b), the trends of DR with $\mathrm{Re}_\tau$ lie between that of small-eddy and large-eddy actuation. For $\mathrm{Re}_\tau \leq 2000$, DR $\approx 8\%$ for both sets of actuation parameters. As $\mathrm{Re}_\tau$ increased to 9,700, the drag reduction for the first set of actuation parameters ($A^+ = 7.8$) increased to a level between 13% and 16%. The second set of intermediate actuation parameters using a lower oscillation amplitude ($A^+ = 4.9$) was similarly able to generate DR $= 9.5\%$ drag reduction at $\mathrm{Re}_\tau = 6{,}000$.

### Effect of actuation on near-wall turbulence

To better understand these results, consider the power spectral density of the wall shear stress ($\phi^+_{\tau\tau}$). For the non-actuated cases, as seen earlier in Figure 2, a strong peak in the spectrum is located at $T^+ \approx 100$, which reflects the intense high-frequency turbulence generated by the near-wall streaks. For the small-eddy actuation, shown in Figure 5(a), we observe a broadband attenuation of the wall stress fluctuations in addition to an overall reduction in the mean stress (i.e, DR $\approx 25\%$ from Figure 4a). Specifically, the small-eddy actuation was observed to severely attenuate all scales for $T^+ < 1{,}000$, while shifting the spectrum towards shorter time scales.

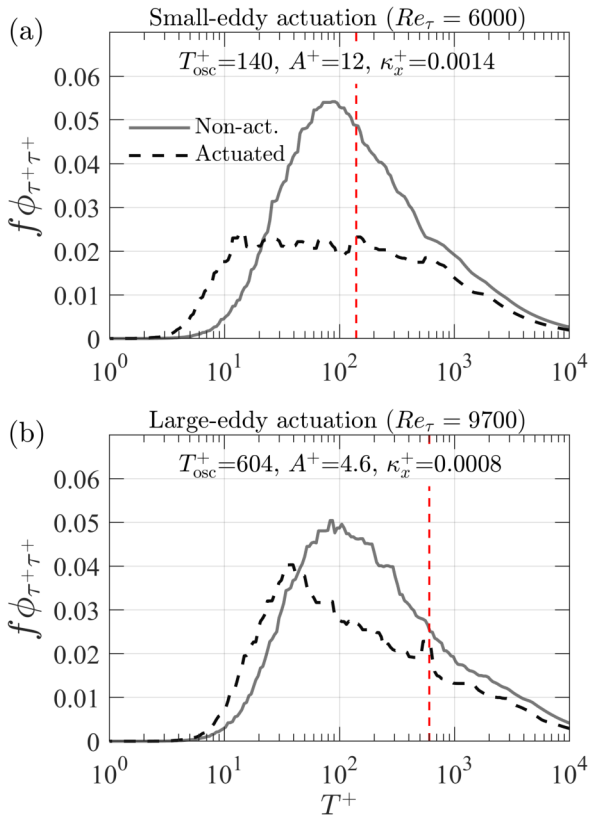


**Figure 5:** Pre-multiplied $\tau_w-$ spectra $(f^+\phi^+_{\tau\tau})$ as a function of time scale, $T^+$, with and without actuation for (a) small-eddy parameters at $\mathrm{Re}_\tau = 6{,}000$ and (b) large-eddy actuation parameters at $\mathrm{Re}_\tau = 9{,}700$. Spectra for flow without actuation are shown in solid gray. Spectra with small-eddy and large-eddy actuation are shown in dashed black lines, respectively. Vertical dashed lines indicate the inner-scaled period of actuation, $T^+_{osc}$.

Figure 5(b) shows the same comparison for one of the large-eddy actuation sets $[A^+ \approx 5, T^+_{\mathrm{osc}} \approx 600, \kappa^+_x = 0.0008]$ at $\mathrm{Re}_\tau = 9{,}700$ where DR $\approx 13\%$ (see the circle in Figure 4c). Here, despite the lower oscillation frequency, the large-eddy actuation similarly attenuates the contributions from a broad band of turbulent motions for $50 \lesssim T^+ \lesssim 2{,}000$, while high-frequency motions of $T^+ \lesssim 50$ were nearly unaffected. Clearly, the action of large-eddy actuation is not confined to the large-scale contributions. This feature, combined with substantial DR (ref. Figure 4c), indicates that large-eddy actuation can be an effective alternate pathway for suppressing the wall stress at higher Reynolds numbers.

Visualizations from LES at low Reynolds numbers can also be helpful in interpreting the underlying mechanisms of drag reduction. In the case of small-eddy actuation, the parameters adopted in the present investigation $[A^+ = 12, T^+_{osc} = 140, \kappa^+_x = 0.0014]$ were near-optimal for targeting the statistically significant near-wall streaks at both high and low Reynolds numbers (see the persistent motions in Figure 6a). This was accomplished by matching the time-period of oscillation $T_{osc}$ with the time-scale of the streaks, $T^+ \approx 100$. The universality of these streaks allows their actuation to be an effective control strategy across a wide range of Reynolds numbers as evidenced by the Reynolds number invariant peak in the $\tau_w$-spectra.

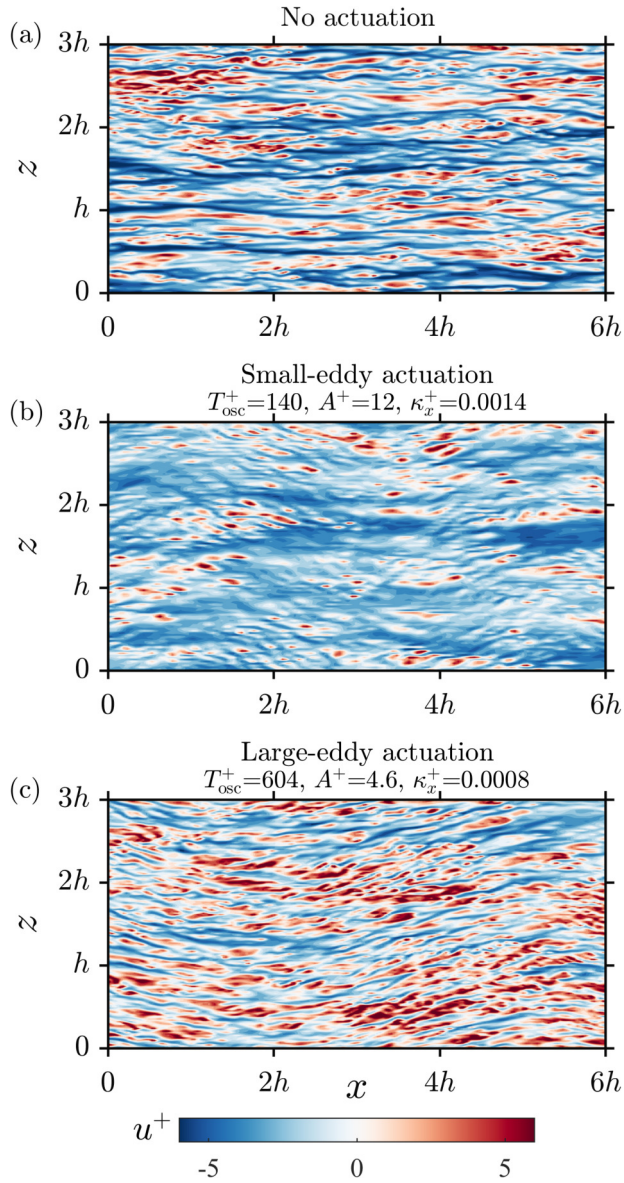


**Figure 6:** Visualizations of near-wall turbulence computed by LES in channel flow illustrating the effects of actuation at $\mathrm{Re}_\tau = 951$ ($h$ is the height of the channel). Contours of the streamwise velocity fluctuations ($u^+$) at $y^+ \approx 12$ are shown with (a) no actuation, (b) small-eddy actuation and (c) large-eddy actuation matching the actuation parameters shown in Figure 5(a) - (b) at high $\mathrm{Re}_\tau$. Images are adapted from Marusic et al. (2021).

The flow visualization at $\mathrm{Re}_\tau = 951$ shown

in Figure 6(b) demonstrates how small-eddy actuation depletes the near-wall streaks and thereby significantly reduces the intensity of turbulence near the wall. This behavior was echoed in the $\tau_w$-spectra measured at $\mathrm{Re}_\tau =$ 6,000 (Figure 5a), where there was significant attenuation of the near-wall streaks centered around $T^+ \approx 100$, and even some attention of larger scale energy ($T^+ > 350$).

Unlike small-eddy actuation, the turbulent scales perturbed by large-eddy actuation are Reynolds number dependent. As seen from Figure 2, the turbulent scales that match the time period of large-scale actuation, $T^+_{osc} =$ 600 and 1,100, carry negligible energy at $\mathrm{Re}_\tau =$ 1,000. Consequently, this actuation strategy at low Reynolds numbers fails to break up the near-wall structures and attenuate their intensity, as shown in Figure 6(c). Instead, the structures merely meander passively following the traveling wave at the wall. However, at high Reynolds numbers (e.g., $\mathrm{Re}_\tau \gtrsim 10^4$), the large-scale actuation strategy becomes effective because reasonably energetic motions are present at $T^+ \gtrsim 600$. In fact, Figure 5(b) demonstrates that large-scale actuation at $\mathrm{Re}_\tau =$ 9,700 attenuates the energy across a broad range of scales, even for scales far smaller than $T^+_{osc}$, and with a relatively modest value of $A^+ = 4.6$.

Hutchins and Marusic (2007) and Mathis et al. (2009) showed that the relative contribution of the large-scale footprint to the total skin-friction drag increases from roughly $8\%$ at $\mathrm{Re}_\tau \approx 1000$ to about $20 - 30\%$ at $\mathrm{Re}_\tau \approx 10^4 - 10^5$, and that the large-scale events modulate the amplitude of small-scale events near the wall. The two-way coupling between large-scales and small-scales that are prominent at high Reynolds numbers are not accounted for in the low-Reynolds-number-based predictions of drag reduction. The current results emphasize the importance of understanding and leveraging the large-scale physics when designing any control strategy for drag reduction in high-Reynolds-number turbulent flow.

### Estimated Net Power Savings

While drag reduction is an important performance parameter, the relevant efficiency of active flow control for transportation applications is best determined from the net power saving (NPS).

Here, we define NPS as the percent difference between the total power required for the non-actuated case ($P^+_0$) and the oscillating case ($P^+ + P^+_{\mathrm{in}}$), and it is given by:

$$\mathrm{NPS} = \frac{P^+_0 - (P^+ + P^+_{\mathrm{in}})}{P^+_0} = \mathrm{DR} - \frac{P^+_{\mathrm{in}}}{P^+_0}. \quad (8)$$

The pumping powers $P^+_0$ and $P^+$ required to drive the flow over the stationary wall and oscillating wall are given by $P^+_0 = U^+_{b_0}$ and $P^+ = (1 - \mathrm{DR})U^+_{b_0}$, respectively, where $U^+_{b_0}$ is the bulk velocity of the stationary case. The input power to the flow required for the actuation ($P^+_{\mathrm{in}}$) can be computed from the integral:

$$P^+_{\mathrm{in}} = \frac{1}{T^+_{\mathrm{avg}} L^+_x L^+_z} \int_{t^+}^{t^+ + T^+_{\mathrm{avg}}} \int_0^{L^+_x} \int_0^{L^+_z} w_s{}^+ \left( \frac{\partial w^+}{\partial y^+}\Big|_{y^+=0} \right) dx^+ dz^+ dt^+. \quad (9)$$

Here, $T^+_{\mathrm{avg}}, L^+_x, L^+_z$ are the averaging time, streamwise and spanwise domain lengths, respectively; $w^+_s \equiv w^+\big|_{y^+=0}$, $\partial w^+/\partial y^+\big|_{y^+=0}$ are the instantaneous spanwise velocity and its wall-normal gradient at the wall ($y^+ = 0$), respectively.

The integral in Equation 8 can be calculated for the LES results, but the experiments could not resolve the instantaneous spanwise velocity gradient at the wall, $\partial w^+/\partial y^+\big|_{y^+=0}$. Instead, we use the laminar generalized Stokes layer (GSL) model developed by Quadrio and Ricco (2011) to estimate the instantaneous spanwise velocity profile near the wall according to

$$w^+(x^+, y^+, t^+) = A^+ \mathcal{R}\left\{ C e^{i(k^+_x x^+ - \omega^+ t^+)} \mathrm{Ai}\left[ e^{\pi i/6} \left(k^+_x [1 - \mathrm{DR}]\right)^{1/3} \left( y^+ - \frac{\omega^+}{k^+_x [1 - \mathrm{DR}]} - \frac{i k^+_x}{1 - \mathrm{DR}} \right) \right] \right\} \quad (10)$$

where

$$C = \left\{ \mathrm{Ai}\left[ i e^{i\pi/3} \left(k^+_x [1 - \mathrm{DR}]\right)^{1/3} (\omega^+/k^+_x + i k^+_x)/[1 - \mathrm{DR}] \right] \right\}^{-1}.$$

Ai is the Airy function of the first kind, and $\mathcal{R}\{...\}$ is the real part of the argument. This model allows us to estimate the input power from the spanwise oscillation for each set of flow and actuation parameters. Gatti and Quadrio (2013) evaluated the fidelity of this approach by comparing values of $P^+_{\mathrm{in}}/P^+_0$ computed using $w^+$ from their DNS with those determined from Equation (10) and found excellent agreement.

A similar comparison between the power estimates from the current LES results and the GSL model also yielded a good agreement, where the maximum difference in $P^+_{\mathrm{in}}/P^+_0$ was less than $1\%$ for the large-eddy actuation cases, and less than $3\%$ for the small-eddy actuation cases. Using Equations 8, 9, and 10, $P^+_{\mathrm{in}}$ and NPS could be estimated for the different actuation schemes. As in Figure 4, we show the NPS as a function of $\mathrm{Re}_\tau$ for the small-eddy, intermediate, and large-eddy actuation parameters in Figure 7(a)-(c), respectively.

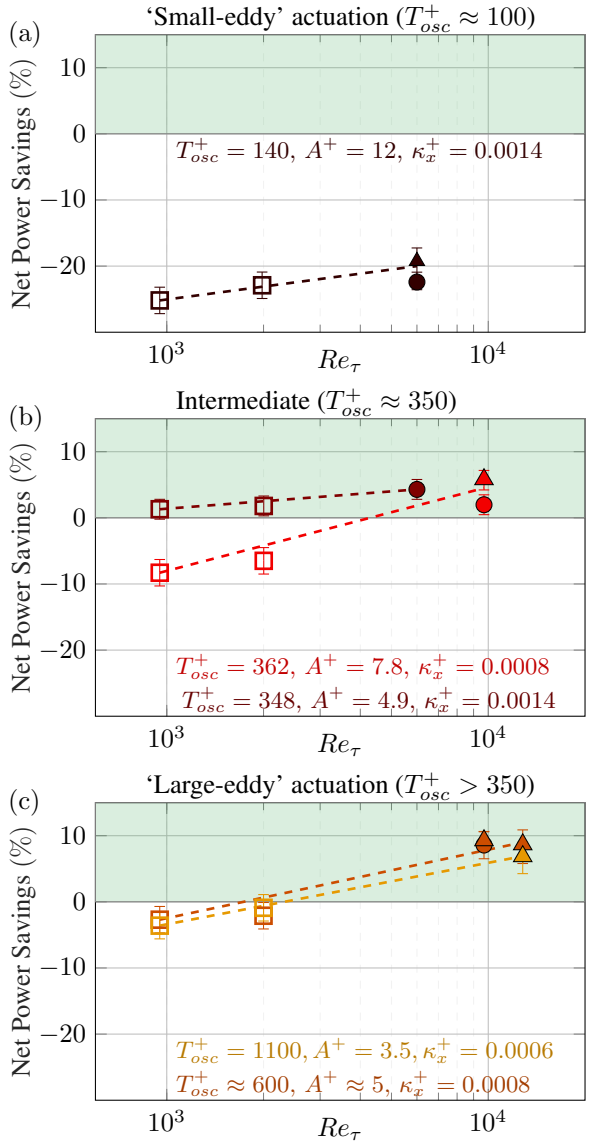


**Figure 7:** Estimated Net Power Savings (%) as a function of $\mathrm{Re}_\tau$ using (a) 'small-eddy', (b) intermediate, and (c) 'large-eddy' actuation parameters. (□): LES results; (●): hot-wire measurements; (▲): drag balance results. Green-shaded area indicates the region of positive net power savings (NPS $>$ 0). Error bars indicate one standard deviation estimated uncertainty ranges based on average measurements from independent experiments. Dashed lines (– –) connecting experimental and computational results serve as a visual aid only. Figures are adapted from Marusic et al. (2021).

Though the small-eddy actuation provided the largest drag reduction (DR $\geq$ 25%), we can see from Figure 7(a) that this level of drag reduction comes at a substantial cost in power, incurring a net power penalty between NPS $= -27\%$ and NPS $= -20\%$ for 951 $\leq \mathrm{Re}_\tau \leq 6,000$. From an analysis of Equation 10, one can show that the power needed to drive the Stokes layer by an oscillating surface scales as $P_{\mathrm{in}} \propto \omega^{5/2}$ (Quadrio and Ricco, 2011). This power requirement, in turn, scales as $P_{\mathrm{in}} \propto (\mathrm{Re}_\tau\, u_{\tau 0}/\delta)^{5/2}$ in our experiments for actuation frequencies matched those of the near-wall small eddies, i.e., small-eddy actuation. Thus, the considerably lower frequencies required for large-eddy actuation compared to small-eddy actuation at high Reynolds numbers enable significantly reduced power costs. For example, at $\mathrm{Re}_\tau =$ 12,800 in the wind tunnel, as $T^+_{\mathrm{osc}}$ increases from 100 to 1,000, the corresponding frequency of oscillation drops from 150 Hz to 15 Hz, greatly reducing actuation power while delivering a drag reduction of about 8%. The consequences of this reduced input power are shown in Figure 7(c), where the net power savings in each large-eddy actuation case was estimated to go from NPS $= -4\%$ at $\mathrm{Re}_\tau = 951$ up to NPS $\approx +10\%$ at $\mathrm{Re}_\tau =$ 9,700. In other words, at $\mathrm{Re}_\tau =$ 9,700, the total power cost to pump the flow and oscillate the surface was 10% less than the power used to pump the flow over a stationary surface.

Lastly, for the two intermediate frequencies corresponding to $T^+_{\mathrm{osc}} \approx 350$, the trends of NPS lie between that of small-eddy and large-eddy actuation (see Figure 7b). At $\mathrm{Re}_\tau \leq 2000$, DR $\approx 8\%$ for both sets of actuation parameters yet we see a marked difference in the NPS. For the first set of actuation parameters ($A^+ = 7.8$) we find NPS $\approx -8\%$ at $\mathrm{Re}_\tau \leq$ 2,000, but NPS $= 2 - 6\%$ at $\mathrm{Re}_\tau =$ 9,700. For the second set of actuation parameters using a lower oscillation amplitude ($A^+ = 4.9$) we maintain NPS $= 1{-}5\%$ for $951 \leq \mathrm{Re}_\tau \leq 6,000$. The variation in NPS with $A^+$ highlights the importance of further decoupling the roles of the various actuation parameters and fully characterizing the multi-dimensional parameter space.

## CONCLUSIONS

The findings have several important implications for high-Reynolds-number drag reduction strategies. First, we were able to generate drag reduction at high Reynolds numbers across a wide array of actuation conditions. When the flow was actuated parameters with parameters comparable to the near-wall motions (i.e., small-eddy actuation), we found good agreement between our observed $\mathrm{Re}_\tau$-trend and the log-law offset predictions of Gatti and Quadrio (2016). This agreement implies that spanwise wall oscillations strategies designed to target the near-wall structures could be more effective for reducing drag at higher Reynolds numbers than many previously thought (Hurst et al., 2014; Choi et al., 2002; Ricco and Quadrio, 2008; Touber and Leschziner, 2012).

Furthermore, we observed that considerable drag reduction could be achieved with much lower actuation frequencies (i.e., large-eddy actuation), and that this actuation strategy exhibits an increasing trend with Reynolds number over the range investigated here.

Although low-frequency actuation produces negligible drag reduction at low Reynolds numbers, it was found to generate $\mathrm{DR} = 8 - 13\%$ and $\mathrm{NPS} \approx 8\%$ at $\mathrm{Re}_\tau \approx 10^4$. These findings challenge much of the understanding around this actuation method, where drag reduction was believed to always degrade with Reynolds number. While it is highly encouraging to find that the effects of large-eddy actuation are broadband, there are numerous questions around the precise mechanisms and dynamics that allows these energy transfers between the large and small scales. Exactly how large eddy actuation is able to achieve such broadband attenuation at scales much finer than those of the actuation itself remains an interesting question for future study. Perhaps more relevant for naval applications was the success of this low-frequency actuation in terms of net power savings. The combination of increasing efficacy at high Reynolds numbers and dramatically low input power requirements means that low-frequency actuation presents a potentially promising strategy for future implementations of active drag reduction technologies at high Reynolds number.

The current results emphasize the importance of understanding and leveraging the large-scale physics when designing any control strategy for drag reduction in high-Reynolds-number turbulent flow. In practical terms, a moving surface is likely impractical for most naval applications. However, similar actuation effects could possibly be achieved without the need for moving parts. One example is the use of a seawater Lorentz body force driven by either electric or magnetic field sources such as those proposed by Du and Karniadakis (2000). Our insights on small- and large-eddy actuation can also inform the design of a new class of passive drag reducing surfaces. For example, traditional (i.e., riblets) and modern (e.g., superhydrophobic and liquid-infused surfaces) approaches to passive drag reduction typically target and perturb the near-wall structures and motions. This approach is well-understood and modeled in the literature but remains practically challenging to implement over large areas at high Reynolds number. Instead, new surfaces could be designed to target large-scale structures, presenting a potentially new approach for passive drag reduction design.

## ACKNOWLEDGEMENTS

Funding for this research was provided by the Deep Science Fund of Intellectual Ventures. The authors would like to thank the Scientific Instrument Manufacturing and Test Group at Intellectual Ventures Laboratory for designing and fabricating the SATB, Wayt Gibbs for his helpful comments, and Geoff Duke for his assistance with the SATB. Computing resources were provided through the Spartan High-Performance Computing service at The University of Melbourne, the Pawsey Supercomputing Centre and the National Computing Infrastructure (NCI) program with funding from the Australian Government and the Government of Western Australia.

## REFERENCES

Agostini, L. and Leschziner, M., "The impact of footprints of large-scale outer structures on the near-wall layer in the presence of drag-reducing spanwise wall motion," Flow, Turbulence and Combustion, Vol. 100, No. 4, 2018, pp. 1037–1061.

Agostini, L. and Leschziner, M., "On the departure of near-wall turbulence from the quasi-steady state," Journal of Fluid Mechanics, Vol. 871, 2019, p. R1.

Auteri, F., Baron, A., Belan, M., Campanardi, G., and Quadrio, M., "Experimental assessment of drag reduction by traveling waves in a turbulent pipe flow," Phys. Fluids, Vol. 22, No. 11, nov 2010, ISSN 10706631.

Baars, W.J., Squire, D.T., Talluru, K.M., Abbassi, M.R., Hutchins, N., and Marusic, I., "Wall-drag measurements of smooth-and rough-wall turbulent boundary layers using a floating element," Exp. Fluids, Vol. 57, No. 5, 2016, p. 90.

Bird, J., Santer, M., and Morrison, J.F., "Compliant kagome lattice structures for generating in-plane waveforms," Int. J. Solids Struct., Vol. 141, 2018a, pp. 86–101.

Bird, J., Santer, M., and Morrison, J.F., "Experimental control of turbulent boundary layers with in-plane travelling waves," Flow Turbul. Comb., Vol. 100, No. 4, 2018b, pp. 1015–1035.

Cattafesta, L. and Sheplak, M., "Actuators for active flow control," Annu. Rev. Fluid Mech., Vol. 43, 2011, pp. 247–272.

Chandran, D., Monty, J.P., and Marusic, I., "Spectral-scaling-based extension to the attached eddy model of wall turbulence," Phys. Rev. Fluids, Vol. 5, Oct 2020, p. 104606.

Choi, J.I., Xu, C.X., and Sung, H.J., "Drag reduction by spanwise wall oscillation in wall-bounded turbulent flows," AIAA J., Vol. 40, No. 5, 2002, pp. 842–850, ISSN 00011452.

Choi, K.S. and Graham, M., "Drag reduction of turbulent pipe flows by circular-wall oscillation," Phys. Fluids, Vol. 10, No. 1, 1998, pp. 7–9.

Chung, D., Marusic, I., Monty, J.P., Vallikivi, M., and Smits, A.J., "On the universality of inertial energy in the log layer of turbulent boundary layer and pipe flows," Exp. Fluids, Vol. 56, No. 7, 2015, pp. 1–10.

Chung, D., Monty, J.P., and Ooi, A., "An idealised assessment of Townsend's outer-layer similarity hypothesis for wall turbulence," J. Fluid Mech., Vol. 742, 2014.

Del Álamo, J.C., Jiménez, J., Zandonade, P., and Moser, R.D., "Scaling of the energy spectra of turbulent channels," J. Fluid Mech., Vol. 500, No. 500, feb 2004, pp. 135–144, ISSN 00221120.

Du, Y. and Karniadakis, G.E., "Suppressing wall turbulence by means of a transverse traveling wave," Science, Vol. 288, No. 5469, may 2000, pp. 1230–1234, ISSN 00368075.

Fukagata, K., Kasagi, N., and Koumoutsakos, P., "A theoretical prediction of friction drag reduction in turbulent flow by superhydrophobic surfaces," Phys. Fluids, Vol. 18, No. 5, 2006, p. 051703.

Gatti, D. and Quadrio, M., "Performance losses of drag-reducing spanwise forcing at moderate values of the Reynolds number," Phys. Fluids, Vol. 25, No. 12, 2013, p. 125109.

Gatti, D. and Quadrio, M., "Reynolds-number dependence of turbulent skin-friction drag reduction induced by spanwise forcing," J. Fluid Mech., Vol. 802, 2016, pp. 553–582.

Germano, M., Piomelli, U., Moin, P., and Cabot, W.H., "A dynamic subgrid-scale eddy viscosity model," Phys. Fluids, Vol. 3, 1991, pp. 1760–1765.

Hurst, E., Yang, Q., and Chung, Y.M., "The effect of Reynolds number on turbulent drag reduction by streamwise travelling waves," J. Fluid Mech., Vol. 759, nov 2014, pp. 28–55, ISSN 14697645.

Hutchins, N. and Choi, K.S., "Accurate measurements of local skin friction coefficient using hot-wire anemometry," Prog. Aerosp. Sci., Vol. 38, No. 4-5, 2002, pp. 421 – 446.

Hutchins, N. and Marusic, I., "Large-scale influences in near-wall turbulence," Phil. Trans. R. Soc. A, Vol. 365, 2007, pp. 647–664.

Iwamoto, K., Fukagata, K., Kasagi, N., and Suzuki, Y., "Friction drag reduction achievable by near-wall turbulence manipulation at high Reynolds numbers," Phys. Fluids, Vol. 17, No. 1, 2005, pp. 011702–011702.

Jiménez, J., "Coherent structures in wall-bounded turbulence," J. Fluid Mech., Vol. 842, 2018, p. P1.

Jung, W.J., Mangiavacchi, N., and Akhavan, R., "Suppression of turbulence in wall-bounded flows by high-frequency spanwise oscillations," Physics of Fluids A: Fluid Dynamics, Vol. 4, No. 8, 1992, pp. 1605–1607.

Leschziner, M.A., Choi, H., and Choi, K.S., "Flow-control approaches to drag reduction in aerodynamics: progress and prospects," Phil. Trans. R. Soc. A, Vol. 369, No. 1940, apr 2011, pp. 1349–1351, ISSN 1364-503X.

Lilly, D.K., "A proposed modification of the Germano subgrid-scale closure method," Phys. Fluids, Vol. 4, 1992, pp. 633–635.

Marusic, I., Chandran, D., Rouhi, A., Fu, M.K., Wine, D., Holloway, B., Chung, D., and Smits, A.J., "An energy-efficient pathway to turbulent drag reduction," Nature Communications, Vol. 12, No. 1, oct 2021, pp. 1–8, ISSN 2041-1723.

Marusic, I., Mathis, R., and Hutchins, N., "Predictive model for wall-bounded turbulent flow," Science, Vol. 329, No. 5988, 2010, pp. 193–196.

Mathis, R., Hutchins, N., and Marusic, I., "Large-scale amplitude modulation of the small-scale structures in turbulent boundary layers," J. Fluid Mech., Vol. 628, 2009, pp. 311–337.

Mathis, R., Marusic, I., Chernyshenko, S.I., and Hutchins, N., "Estimating wall-shear-stress fluctuations given an outer region input," J. Fluid Mech., Vol. 715, 2013, p. 163.

Meysonnat, P.S., Roggenkamp, D., Li, W., Roidl, B., and Schröder, W., "Experimental and numerical investigation of transversal traveling surface waves for drag reduction," Eur. J. Mech. B Fluids, Vol. 55, 2016, pp. 313–323.

Nakanishi, R., Mamori, H., and Fukagata, K., "Relaminarization of turbulent channel flow using traveling wave-like wall deformation," Int. J. Heat Fluid Flow, Vol. 35, 2012, pp. 152–159.

Quadrio, M. and Ricco, P., "The laminar generalized Stokes layer and turbulent drag reduction," J. Fluid Mech., Vol. 667, 2011, pp. 135–157.

Quadrio, M., Ricco, P., and Viotti, C., "Streamwise-travelling waves of spanwise wall velocity for turbulent drag reduction," J. Fluid Mech., Vol. 627, 2009, pp. 161–178.

Ricco, P. and Quadrio, M., "Wall-oscillation conditions for drag reduction in turbulent channel flow," Intl J. Heat Fluid Flow, Vol. 29, No. 4, aug 2008, pp. 601–612, ISSN 0142727X.

Ricco, P., Skote, M., and Leschziner, M.A., "A review of turbulent skin-friction drag reduction by near-wall transverse forcing," Progress in Aerospace Sciences, Vol. 123, may 2021, p. 100713.

Schoppa, W. and Hussain, F., "A large-scale control strategy for drag reduction in turbulent boundary layers," Phys. Fluids, Vol. 10, No. 5, 1998, pp. 1049–1051.

Schultz, M., Bendick, J., Holm, E., and Hertel, W., "Economic impact of biofouling on a naval surface ship," Biofouling, Vol. 27, No. 1, 2011, pp. 87–98.

Skote, M., Mishra, M., and Wu, Y., "Wall oscillation induced drag reduction zone in a turbulent boundary layer," Flow Turbul. Comb., Vol. 102, No. 3, 2019, pp. 641–666.

Smits, A.J., McKeon, B.J., and Marusic, I., "High Reynolds number wall turbulence." Annu. Rev. Fluid Mech., Vol. 43, 2011, pp. 353–375.

Tomiyama, N. and Fukagata, K., "Direct numerical simulation of drag reduction in a turbulent channel flow using spanwise traveling wave-like wall deformation," Phys. Fluids, Vol. 25, No. 10, 2013, p. 105115.

Touber, E. and Leschziner, M.A., "Near-wall streak modification by spanwise oscillatory wall motion and drag-reduction mechanisms," J. Fluid Mech., Vol. 693, Feb 2012, pp. 150–200, ISSN 00221120.

Viotti, C., Quadrio, M., and Luchini, P., "Streamwise oscillation of spanwise velocity at the wall of a channel for turbulent drag reduction," Phys. Fluids, Vol. 21, No. 11, 2009, p. 115109.

Yakeno, A., Hasegawa, Y., and Kasagi, N., "Modification of quasi-streamwise vortical structure in a drag-reduced turbulent channel flow with spanwise wall oscillation," Phys. Fluids, Vol. 26, No. 8, aug 2014, ISSN 10897666.

Yao, J., Chen, X., and Hussain, F., "Reynolds number effect on drag control via spanwise wall oscillation in turbulent channel flows," Physics of Fluids, Vol. 31, No. 8, aug 2019, ISSN 10897666.

## DISCUSSION

Michael P. Schultz
U.S. Naval Academy
Dept. of Naval Arch. & Ocean Eng.
590 Holloway Road, Annapolis, MD 21402
Ph: 410.293.6440
mschultz@usna.edu

The authors should be congratulated for a most inspiring paper on drag reduction at high Reynolds number. They have conducted incredibly challenging experiments and elegant computations. As a result, the reader is left with a better understanding of the mechanisms of turbulent drag reduction. As an experimentalist, for more than a decade I have been fascinated by the streamwise traveling wave approach to reducing drag. However, I felt that it would be difficult or impossible to realize experimentally. The present authors have not only done it but have also showed us a new avenue for drag reduction that scales favorably with Reynolds number. This is a very exciting finding!

In the paper, compelling evidence of net drag reduction using low frequency forcing to affect the large-scale eddies is presented. Do the authors have any thoughts on how persistent the drag reduction downstream of the actuation might be?

The width of the slats used to create the streamwise traveling wave would seem to be an important parameter. Was the slat width that was used in the present experiments guided by previous computations? Is it 'optimized' in any sense?

The authors mention avenues to exploit the present findings using non-mechanical means via an active (e.g. Lorentz forcing) or passive (e.g. riblets, superhydrophobic or liquid-infused surfaces) approach. Have the authors given much thought on what such a passive surface might look like?

## AUTHOR'S REPLY

Thank you, Prof. Schultz, for the very insightful observations, comments and questions.

Regarding your first question, determining how persistent the drag reduction is downstream of the actuation remains an ongoing area of research for the authors. Preliminary experimental results conducted for the small-eddy and intermediate actuation regimes indicate that the flow recovers from the actuation after approximately 3000 viscous units downstream of the actuator. This recovery length is consistent with the observations of Ricco and Wu (2004) and Skote et al. (2019) who considered small-eddy actuation at $T^+_{osc} = 67$. The authors expect and hope that the effects of large-eddy actuation are more persistent downstream due to the longer time scales associated with the large-scale structures. However, this hypothesis still requires experimental validation.

Regarding the width of the slats, this parameter was informed by a combination of practical and dynamical considerations. The sinusoidal traveling wave was discretized with six slats constituting a fixed streamwise wavelength $\lambda = 2\pi/\kappa_x = 0.3$ m. The streamwise wavelength was chosen to be approximately the boundary thickness at the streamwise location of the SATB. Following the analysis of Auteria et al. (2010), six slats were found to be sufficient to approximate sinusoidal motion with minimal discretization effects while still keeping the mechanical complexity of the system tractable. Incidentally, this 5 cm width corresponds to $\mathcal{O}(10^3)$ viscous units, which is nominally the length of the near wall streaks. This coincidence could potentially be playing a role in the drag reduction, but further investigation is necessary to evaluate this idea.

Lastly, regarding the design of passive devices, the authors do not have specific designs and implementations in mind at this time. The primary motivation of this study is to demonstrate that attenuating large scale structures can provide drag reduction that has not been captured by existing modelling approaches. The authors hypothesize that replicating the effect is likely possible through combination of tailored surface morphology or slip surfaces. However, whether the drag reduction effects from this mechanism would exceed any parasitic drag remains an open question.

## DISCUSSION

William Devenport
Virginia Tech
Center for Engineering and Research in Aerohydrodynamic Technologies (CREATe)
660 McBryde Hall, Blacksburg, VA 24060
Ph 540.231.4456
devenport@vt.edu

I very much enjoyed reading this clear and convincing account of a careful and important study. I am in awe of experimental care that this study must have taken.

The authors are able to directly observe the effects of the small-eddy actuation in suppressing near-wall streaks, but the limits of the LES Reynolds number prevent them observing the exact mechanism by which large-eddy actuation is effective. Since large eddy actuation does not influence the high-frequency portion of the wall shear stress spectrum, the implication is that near-wall streaks are not involved here. Would the authors care to speculate on the mechanism involved?

Could the authors comment on the effects on the wall shear stress spectrum of the slowest wall motions at $T^+_{osc} = 1100$ studied with the highest $Re_\tau = 12800$ flow? Compared to Figure 5(b) does the attenuation of the spectrum shift rightward with the actuation frequency (implying that, as Re increases further, actuation frequency could be further reduced) or remain fixed?

## AUTHOR'S REPLY

Thank you, Prof. Devenport, for the very insightful observations, comments and questions. You have raised essential, yet unresolved, questions that are of keen interest to the authors. Regarding the mechanism of large-eddy actuation and as you correctly note, the authors are only able to infer the mechanism of drag reduction through the experimental results versus the LES simulations. Though the large-eddy actuation isn't as effective at attenuating the near high-frequency motions as the small-eddy or intermediate actuation, the effects of the large-eddy actuation are surprisingly broadband, extending to motions smaller than $T^+ \approx 100$. While this feature is highly encouraging for the efficacy of this approach, there are still numerous questions around the precise mechanisms and dynamics that enable this energy transfer between the large and small scales. Addressing these questions remains an ongoing area of research for the authors.

Regarding the effects on the wall shear stress spectrum from large-eddy actuation ($T^+_{osc} = 1100$) at $Re_\tau = 12800$, there unfortunately are no hotwire data for those flow conditions, only drag balance data. Comparable measurements at $Re_\tau = 9700$ for $T^+_{osc} = 906$ do exist as part of the current dataset and are included below in Figure 1. There, we present the difference between the large-eddy actuated $\tau_w-$spectra and the non-actuated reference $\tau_w-$spectra at $Re_\tau = 9700$ for two different cases: $T^+_{osc} = 604$ ($A^+ = 4.6$) and $T^+_{osc} = 906$ ($A^+ = 3$). In the latter case, despite the lower frequency of oscillation, the effects are still broadband. Compared to the $T^+_{osc} = 604$ case, the overall effects of the $T^+_{osc} = 906$ actuation are much less pronounced, especially for time scales larger than the actuation. This effect is most likely due, at least in part, to the lower amplitude, $A^+$ associated with the lower frequency of actuation. As noted in the manuscript, teasing apart the trends of $T^+_{osc}$ from $A^+$ remains difficult, due to their coupled nature in the experiments. Similarly, it is not obvious if there is a rightward spectrum shift as proposed by the discusser, but the difference between $T^+_{osc} = 604$ and $T^+_{osc} = 906$ on a logarithmic scale is equally hard to discern.

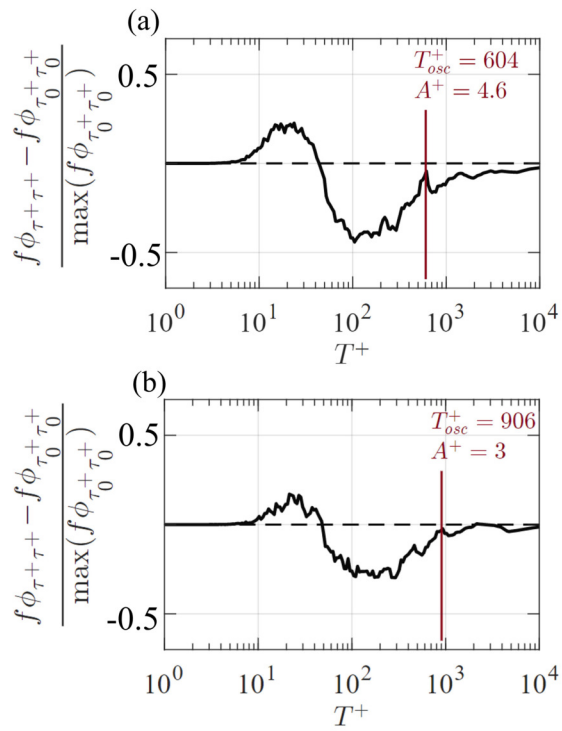


**Figure 1:** Difference between the $\tau_w-$spectra of the large-eddy actuation and the non-actuated (i.e., reference) flow at $Re_\tau = 9700$ for (a) $T^+_{osc} = 604$ ($A^+ = 4.6$) and (b) $T^+_{osc} = 906$ ($A^+ = 3$) normalized by the peak value of the non-actuated spectra. The positive and negative regions indicate energy addition and attenuation, respectively, due to the large-eddy actuation.

## REFERENCES

Auteri, F., Baron, A., Belan, M., Campanardi, G., and Quadrio, M., "Experimental assessment of drag reduction

by traveling waves in a turbulent pipe flow," Phys. Fluids, Vol. 22, No. 11, nov 2010a, ISSN 10706631.

Ricco, P. and Wu, S., "On the effects of lateral wall oscillations on a turbulent boundary layer," Exp. Therm. Fluid Sci., Vol. 29, No. 1, dec 2004, pp. 41–52, ISSN 08941777.

Skote, M., Mishra, M., and Wu, Y., "Wall oscillation induced drag reduction zone in a turbulent boundary layer," Flow Turbul. Comb., Vol. 102, No. 3, 2019, pp. 641–666.